International Journal for Housing Science and Its Applications
Publish August 10, 2025. Volume 46, Issue 4 Pages 3154-3165

https://doi.org/10.70517/ijhsa464261

Research on monitoring stress and deflection under asymmetric loading during bridge construction based on machine vision technology

Zetao Li[1], Jianhua Du[1,2,3,*], Shaohu Jin[1] and Fei Wang[1]

[1] Department of Railway Engineering, Shijiazhuang Institute of Railway Technology, Shijiazhuang, Hebei, 050041, China
[2] Intelligent Control Technology Innovation Center for Bridge and Tunnel Engineering Construction of Hebei Province, Shijiazhuang, Hebei, 050041, China
[3] Application Technology R&D Center of Bridge and Tunnel Intelligent Construction of Hebei Colleges, Shijiazhuang, Hebei, 050041, China

Corresponding authors: (e-mail: lizt_89@163.com).

Abstract Stress and deflection monitoring under asymmetric loading during bridge construction is the core link to ensure structural safety. In this paper, a set of dynamic monitoring and analyzing methods for asymmetric loads is proposed by combining machine vision technology and mechanics theory, and its effectiveness is verified by the engineering case of A bridge. Based on machine vision technology, a four-coordinate system transformation model is established through camera calibration and distortion correction, which eliminates radial and tangential distortion and realizes the accurate restoration of spatial geometric information in the image. In view of the load imbalance between the railroad side and the highway side, the asymmetric cable force mechanics balance equation is established, and the formula for calculating the ratio of the cable force is deduced. Considering the influence of ambient temperature further, a comprehensive calculation method of temperature difference stress in box girder is proposed to quantify the distribution law of temperature difference due to sunshine and cold current and its influence on the longitudinal restraining stress. In the actual engineering verification, by comparing the internal force and stress data of the main pier, such as 50# pier section A bending moment 17075 kN·m and 51# pier-16993 kN·m, the west pier was determined as the force control point, and the top thrust force of 7812 kN was applied. The data analysis shows that the jacking force significantly optimizes the force of the main pier and eliminates the tensile stress of the cross-section, the stress at the upper edge of the A section decreases from 0.83 MPa to -2.12 MPa, and the bending moment adjustment of the main beam reaches 98%, and the reversal of cross-section 1 from -21243 kN·m to 429 kN·m. In addition, the sensitivity analysis of the friction coefficient of the reserved pipeline shows that when the coefficient fluctuation is ± 10%, the maximum displacement difference in the middle span of the main girder in the bridge state is 0.92 mm, indicating that the construction parameters have a significant influence on the deflection.

Index Terms bridge construction, asymmetric loading, stress monitoring, deflection monitoring, asymmetric cable force

I. Introduction

Bridges are the most critical projects in the road transportation system, and they play an extremely important role [1]. With the rapid development of social economy, the scale of bridge construction in China increases year by year, especially the construction of large-span bridges is advancing by leaps and bounds, how to ensure the safety of large-span bridge operation is the current bridge construction industry needs to face the problem, and the monitoring of the stress and deflection under asymmetric loading in the process of bridge construction is an effective measure [2]-[5].

The line displacement of the center of cross-section form along the direction perpendicular to the axis during the bending deformation of the bridge is called deflection, and the disturbance deformation is a key parameter to evaluate the quality of bridge structure in the monitoring process of the bridge, and all kinds of judgments need the accuracy of the static and dynamic disturbance value of the bridge [6]-[9]. Therefore, the disturbance deformation monitoring of bridge structure is an essential measure in the building construction of bridges [10]. Meanwhile, as bridges are subjected to huge loads from transportation means and their own gravity, long-time use and the influence of the natural environment will cause deformation and fatigue of the bridge structure, which in turn will affect its safety and service life [11]-[13].

Therefore, timely and accurate monitoring of the stress of bridge structures can help engineers to understand the health condition of bridges, detect problems in time and take corresponding repair and reinforcement measures,

which is a key step to ensure the safe operation of bridges [14]-[17]. Stress monitoring of bridge structure is to understand the stress condition of bridge structure by measuring the change of its stress state [18]. The application of machine vision technology can be used for non-contact monitoring of stress and deflection under asymmetric loading during bridge construction, and sensors, cameras, and other equipment can be installed around the bridge to monitor the displacement, cracks, and deformation of the building [19]-[22]. At the same time, using image processing technology to analyze the monitored images, it can determine whether the bridge stress and disturbance are stable, discover potential problems in time, and take corresponding measures to repair and protect the safety of the bridge [23]-[25].

With the rapid development of machine vision technology, its advantages of non-contact, high precision and real-time dynamic monitoring provide a new technical path for bridge construction monitoring. In this paper, a systematic asymmetric load monitoring and analysis method is proposed by combining machine vision technology and mechanics theory, aiming at realizing the accurate monitoring of stress and deflection during bridge construction through image data acquisition, mechanics model derivation and environmental factor calculation. Firstly, starting from the camera calibration and aberration correction, which is the core link of machine vision technology, the effect of lens aberration on image data is eliminated through the establishment of a transformation model between the world coordinate system, the camera coordinate system, the image coordinate system and the pixel coordinate system, so as to provide high-precision spatial geometric information for the subsequent analysis. Based on this, the theoretical derivation of asymmetric cable-stayed force partly addresses the problem of load imbalance between the railroad side and the highway side, and establishes a model for calculating the ratio of cable-stayed force through the equilibrium equations of mechanics and the assumption of geometric symmetry and verifies the applicability of the model by combining with the actual engineering parameters. Finally, the temperature difference load calculation of box bridge further considers the influence of ambient temperature change on the structure, and analyzes the temperature difference distribution of single-cell box girder, sunshine and cold flow cooling stress, longitudinal restraining stress, and transverse crack risk respectively, and proposes a comprehensive calculation method of temperature difference stress based on linear and nonlinear corrections.

II. Machine vision-based asymmetric load monitoring method and mechanical analysis for bridge construction

II. A. Camera Calibration and Aberration Correction

When photogrammetric work is performed using machine vision, there are distortions between the camera-acquired image and the original spatial image. In order to obtain accurate spatial image information from the image, the main task of camera calibration is to extrapolate the geometric information of the object in three-dimensional space from the image information acquired by the camera, so as to recognize and reconstruct the spatial object. The relationship between the real coordinates of the spatial object and the pixel coordinates of the corresponding points in the image captured by the camera is determined by the geometric model of the camera imaging, and these geometric model parameters are the camera parameters, and the process of solving the camera parameters is the camera calibration. The process of solving the camera parameters is camera calibration, while distortion correction is the process of using the solved parameters to restore the original information of the captured image.

Camera calibration process involves the main coordinate systems are the world coordinate system, the camera coordinate system, the image coordinate system and the pixel coordinate system, machine calibration of the four coordinate systems shown in Figure 1.

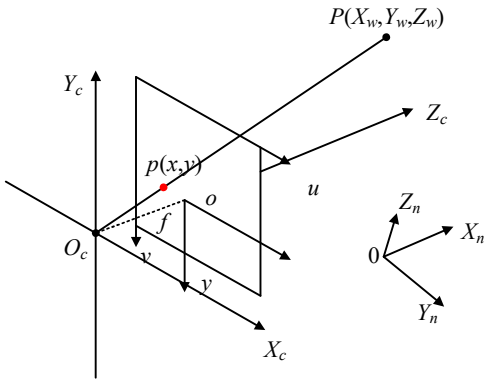

Figure 1: Four coordinate systems calibrated by the camera

The purpose of calibration is to convert the pixel coordinates of an image into actual spatial coordinates so as to restore the real state of the image in space, which is a necessary process for measurement work using machine vision. In short, camera calibration is the process of converting world coordinates into camera coordinates and then into image coordinates, so as to eliminate the errors caused by distortion and obtain accurate measurement results. The relationship between the world coordinate system and the image coordinate system for the point of the same name can be obtained after the conversion of the two coordinate systems, as shown in Equation (1).

$$\begin{bmatrix} u \\ v \\ 1 \end{bmatrix} = K[R \mid t] \begin{bmatrix} x \\ y \\ z \end{bmatrix} \tag{1}$$

where u and v are the coordinates in the image coordinate system, and the unit is mm; x, y, and z are the coordinates in the world coordinate system, and the units are pixels; K is the camera internal reference, which is a $3*3$ matrix, which converts the coordinates from the camera coordinate system to the image coordinate system, and then to the pixel coordinates. R, t is the camera external parameter, R is a $3*3$ matrix, representing the rotational transformation in the x, y, z directions, and t is a $3*1$ matrix, representing the translational transformation in the x, y, z directions.

For general cameras, due to manufacturing accuracy and assembly deviations, the captured images may have aberrations. According to the source of distortion can be divided into radial distortion and tangential distortion, radial distortion is due to the light through the center of the lens, away from the center of the camera lens position of the light than near the center of the position of the light is more likely to be curved, resulting in pixels close to or away from the center of the image plane of the deviation, the deviation of the radius of the lens to the outer circle gradually increases, the common forms of distortion are barrel distortion or occipital distortion as shown in Figure 2. Tangential distortion is due to the lens and the imaging plane is not flat exercise pixel probability of generating deviation, this situation is mostly caused by the lens and chip installation deviation.

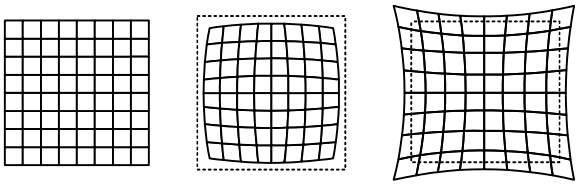

Figure 2: Schematic diagram of radial distortion

Radial aberration as the target becomes farther away from the optical center position, its effect on the imaging effect is also the greater, in order to eliminate the effect of radial aberration, the establishment of k_1, k_2, k_3 three coefficients, and with the Taylor series expansion, can be expressed as equation (2).

$$\begin{cases} x = x'(1 + k_1 r^2 + k_2 r^4 + k_3 r^6) \\ y = y'(1 + k_1 r^2 + k_2 r^4 + k_3 r^6) \end{cases} \tag{2}$$

where, (x, y) are the image coordinates without aberration under the ideal optical center system, (x', y') are the image coordinates in practical applications, and r is the distance from the point to the imaging center. The tangential aberration is schematically shown in Fig. 3.

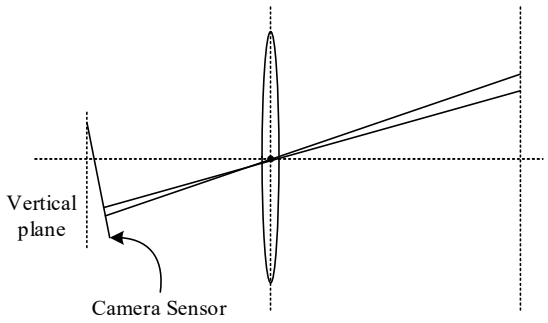

Figure 3: Schematic diagram of tangential distortion

The tangential aberration of the camera is expressed in terms of two parameters P_1 and P_2, then the model expression for the tangential aberration is equation (3).

$$\begin{cases} x = x' + [2P_1x'y' + P_2(r^2 + 2x'^2)] \\ y = y' + [2P_2x'y' + P_1(r^2 + 2y'^2)] \end{cases} \tag{3}$$

According to Eq. (2) and Eq. (3), it can be seen that the superimposed combination of the two aberrations can eliminate the effects brought by both at the same time, and the parameter expression of the superimposed (4).

$$\begin{cases} x = x'(1 + k_1r^2 + k_2r^4 + k_3r^6) + [2P_1x'y' + P_2(r^2 + 2x'^2)] \\ y = y'(1 + k_1r^2 + k_2r^4 + k_3r^6) + [2P_2x'y' + P_1(r^2 + 2y'^2)] \end{cases} \tag{4}$$

Five aberration coefficients in camera calibration can be obtained in Eq. (4), i.e., radial aberration coefficients k_1, k_2, k_3, and tangential aberration coefficients P_1, P_2. In the process of camera calibration, after obtaining the aberration parameter matrix, according to Equation (4) for any output image point (x', y') to calculate its corresponding point (x, y) under the ideal model, and then the pixel point will be assigned to (x', y') for further processing, judging (x', y') as a non-integer is to use interpolation method to calculate the pixel value of the point, and wait for the completion of the processing of all the pixel point After all pixels are processed, the new image is output to realize the correction of image distortion.

II. B. Theoretical derivation of asymmetric cable forces

After completing the calibration and distortion correction of the camera, the spatial geometric information of the image data can be accurately restored, which lays the foundation for the subsequent mechanical analysis of the asymmetric load. Based on this, the study further proposes a theoretical derivation method of the asymmetric cable force for the problem of uneven load distribution between the railroad side and the highway side in bridge construction.

The torsion between the railroad side and the highway side is eliminated by controlling the vertical deflections of the railroad side and the highway side equally, so that the main girder section reaches the equilibrium state as shown in Fig. 4. Then the cable force on the railroad side and the highway side on the same section satisfies the following two conditions: the vertical component force of the diagonal cable on both sides of the railroad and the public side is balanced with the constant load of the main girder; the torque generated by the asymmetric vertical component force of the diagonal cable is balanced with the torque generated by the asymmetric constant load. According to the above two balance conditions, the mechanical balance equation (5) is obtained.

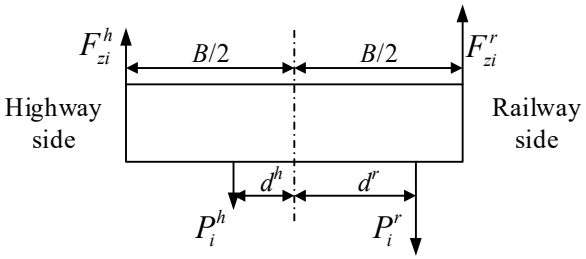

Figure 4: The vertical balance of the main beam section

$$\begin{cases} \sum F_{zi} = 0 \\ \sum T_{xi} = 0 \end{cases} \Rightarrow \begin{cases} F_{zi}^r + F_{zi}^h = \sum P_{zi}^r + \sum P_{zi}^h \\ (F_{zi}^r - F_{zi}^h)B = 2\left(\sum P_{zi}^r d^r - \sum P_{zi}^h d^h\right) \end{cases} \tag{5}$$

Solve equation (5) to get:

$$\begin{cases} T_i^h = \dfrac{F_{zi}^h}{\sin\gamma_i^h} = \dfrac{\left(\sum P_{zi}^r + \sum P_{zi}^h\right)B - 2\left(\sum P_{zi}^r d^r - \sum P_{zi}^h d^h\right)}{2B\sin\gamma_i^h} \\ T_i^r = \dfrac{F_{zi}^r}{\sin\gamma_i^r} = \dfrac{\left(\sum P_{zi}^r + \sum P_{zi}^h\right)B + 2\left(\sum P_{zi}^r d^r - \sum P_{zi}^h d^h\right)}{2B\sin\gamma_i^r} \end{cases} \tag{6}$$

The geometric position of the diagonal cables is generally symmetric in the cross-bridge direction, so $\sin\gamma_i^h = \sin\gamma_i^r$, then:

$$k_i = \frac{T_i^r}{T_i^h} = 1 + \frac{4\left(\sum P_{zi}^r d^r - \sum P_{zi}^h d^h\right)}{\left(\sum P_{zi}^r + \sum P_{zi}^h\right)B - 2\left(\sum P_{zi}^r d^r - \sum P_{zi}^h d^h\right)} \tag{7}$$

where $\sum P_{zi}^r$ and $\sum P_{zi}^h$ are the dead loads on the railway side and the highway side at the same section of the main beam, respectively. d^r and d^h are the transverse distances from the simplified center of the railway side dead load and the road side dead load to the center line of the main beam, respectively. F_{zi}^r and F_{zi}^h are the vertical components of the railway side cable-stayed cable and the highway side cable-stayed cable at the same section, respectively. T_i^h and T_i^r are the cable forces of the railway side cable-stayed cable and the highway side cable-stayed cable at the same section, respectively. k_i is the ratio of the railway side cable force to the road side cable force $k_i > 1$ at the same section.

For the studied bridge A, the constant load of phase I is 573.28kN/m, the constant load of phase II of the upper deck is 70.12kN/m, the constant load of phase II of the lower railroad side is 107.28kN/m, which is 10.25m away from the centerline of the main girder, and the constant load of phase II of the lower highway side is 40.18kN/m, which is 6.94m away from the centerline of the main girder, and by substituting the above parameters into the Eq. (7), then the railroad side cable force and the ratio of the highway side cable force is 1.71.

$$\begin{aligned} k_i &= 1 + \frac{4\times((107.28\times10.25 + 311.29\times8.81) - (40.18\times7.2 + 311.29\times8.81))}{(107.28 + 311.29 + 40.18 + 311.29)\times35 - 2\times(107.28\times10.25 - 40.18\times6.94)} \\ &= 1.71 \end{aligned} \tag{8}$$

II. C. Calculation of temperature difference loads for box bridges

After determining the asymmetric cable-stress ratio, the mechanical equilibrium of the bridge structure still needs to consider the additional effects brought by the ambient temperature changes. For this reason, the study combines the structural characteristics of box bridges, systematically analyzes the temperature distribution law of single-cell box girders under sunshine and cold flow and its influence on the structural stresses, and further improves the comprehensiveness of the asymmetric load monitoring model.

II. C. 1) Temperature difference loads for single-cell box girders

Assuming that the temperature distribution along the longitudinal direction of the structure is uniform for single-cell box girders during solar heating and cooling, the distribution of temperature difference along the girder height and girder width can be simplified as:

$$\begin{aligned} T(y) &= T_{0y}e^{-c_y y} \\ T(x) &= T_{0x}e^{-c_x x} \end{aligned} \tag{9}$$

where, T_{0y} - temperature difference between the top and bottom of the box girder, T_{0x} - temperature difference between the outer webs of the box girder, c_x, c_y -exponential coefficient.

The distribution of temperature difference of single-compartment box girder in different directions is shown in Fig. 5.

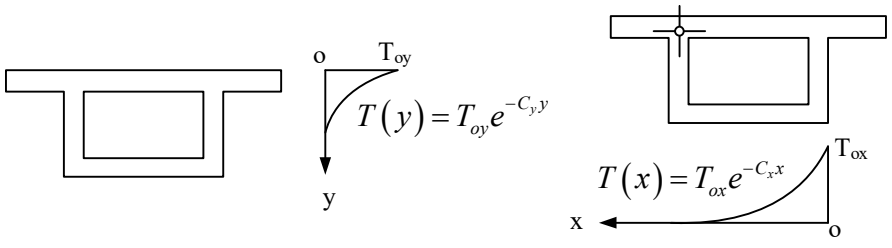

(a) Distribution of temperature difference along the beam height

(b) Distribution of temperature difference along beam width

Figure 5: Temperature distribution of single-chamber box girder in different directions

When the girder is subjected to the cooling effect of cold flow, the distribution of temperature difference in the direction of the thickness of each plate wall of the box girder is calculated as:

$$\overline{T}(y) = \overline{T}_0 e^{-\overline{c}y} \tag{10}$$

where, $\overline{c}$ -exponential coefficient, $\overline{T}_0$ -negative temperature difference of the box girder wall plate, x, y -distance of the calculation point from the outside of the plate (m).

The distribution of cooling temperature difference of cross-section box girder is shown in Fig. 6.

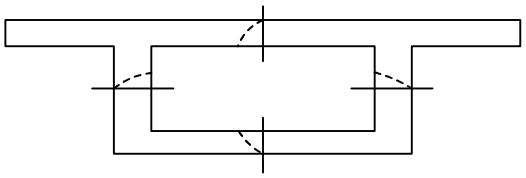

Figure 6: Temperature difference distribution for cooling of cross-sectional box girders

II. C. 2) Calculation of differential temperature stresses in single-cell box girders

(1) Sunshine temperature difference stress

The local temperature difference stress σ_0 of the box girder is simplified by the following equation:

$$\sigma_0 = E(\varepsilon_y - \alpha t_y) \tag{11}$$

$$\varepsilon_y = \varepsilon_1 - \varepsilon_2 \frac{y}{h} \tag{12}$$

Bringing Eq. (12) into Eq. (11) yields:

$$\sigma_0 = E\left(\varepsilon_1 - \varepsilon_2 \frac{y}{h} - \alpha t_y\right) \tag{13}$$

By $\sum N = 0$, it is obtained:

$$\int_b^a (\varepsilon_1 - \varepsilon_2 \frac{y}{h}) b_y dy = \int_b^a \alpha t_y b_y dy \tag{14}$$

is obtained from equation (14):

$$\varepsilon_1 = \frac{\alpha T_0}{F}\left[b\frac{1-e^{-2h}}{a} - b_0\frac{e^{-2a(h-\sigma)}}{a} + 2b_1\frac{1-e^{-2\sigma}}{a}\right] + \frac{n}{h}\varepsilon_2 \tag{15}$$

Similarly, from $\sum M = 0$, we get

$$\int_b^a (\varepsilon_1 - \varepsilon_2 \frac{y}{h})(y-n) b_y dy = \int_b^a \alpha t_y (y-n) b_y dy \tag{16}$$

is obtained from equation (16):

$$\frac{\varepsilon_2}{h} = \beta T_0 [bk_4 - b_0 c_4 + 2b_1 y_4] \tag{17}$$

$$\varepsilon_1 = \frac{\alpha T_0}{F}[bk_4 - b_0 c_4 + 2b_1 y_4] + \frac{n}{h}\varepsilon_2 \tag{18}$$

In the formula:

$$\begin{aligned} &k_1 = \frac{1-e^{-ab}}{a}; k_2 = \frac{1-e^{-ab}(1+ah)}{a^2}; k_3 = \frac{k_2}{k_1}; k_4 = k_1(n-k_3) \\ &c_1 = \frac{e^{-ab} - e^{-a(h-\delta)}}{a}; c_2 = \frac{e^{-ab}(1+a\delta) - e^{-a(h-\delta)}[1+a(h-\delta)]}{a^2} \end{aligned} \tag{19}$$

Get:

$$\varepsilon_1 = \frac{\alpha T_0}{F}[bk_1 - b_0c_1 + 2b\gamma_1] + \frac{\alpha T_0}{I}n[bk_4 - b_0c_4 + 2b\gamma_4] \tag{20}$$

σ_0 from equation (17) equation (18):

$$\sigma_0 = \alpha T_0 E\left\{\frac{1}{F}[bk_1 - b_0c_1 + 2b\gamma_1] + \frac{1}{I}n[bk_4 - b_0c_4 + 2b\gamma_4](n-y) - e^{-ay}\right\} \tag{21}$$

Order:

$$\eta_1 = bk_1 - b_0c_1 + 2b\gamma_1, \eta_2 = bk_4 - b_0c_4 + 2b\gamma_4 \tag{22}$$

Equation (21) can be simplified as:

$$\sigma_0 = \alpha T_0 E\left[\frac{\eta_1}{F} + \frac{\eta_2}{I}(n-y) - e^{-ay}\right] \tag{23}$$

Where, b, h - width of box girder bottom plate and girder height in meters, δ - thickness of the top and bottom plates of the box girder, n - distance from the center of gravity of box girder section to the top surface of the girder, F - cross-sectional area of box girder, b_1 - span of flange on both sides of box girder, b_0 - hollow width of the box girder.

(2) Calculation of cold flow cooling temperature difference stresses

Cold flow in the box girder top and bottom plate produced by the cooling temperature difference stress distribution is inconsistent, engineering calculations often ignored in the cold flow under the influence of temperature difference stress cooling temperature difference stress of the girder body of the smaller cold flow cooling temperature difference stress.

(3) Calculation of longitudinal restraint stress

Most of the prestressed concrete rigid bridges are super-static structures, and the girders will be up-arched when subjected to large temperature difference of sunshine. Due to the limitation of the constraint conditions, the girder will produce a large constraint stress, the value of which is larger than that of the temperature difference constraint stress produced by the static structure, and its large influence cannot be ignored in the construction. The temperature differential confining stresses in such beams can be obtained by multiplying the linear result by a nonlinear correction factor μ_0. For linear problems, they can be calculated by structural mechanics methods.

The calculation procedure for the value of the coefficient μ_0 is shown in Figure 7 below.

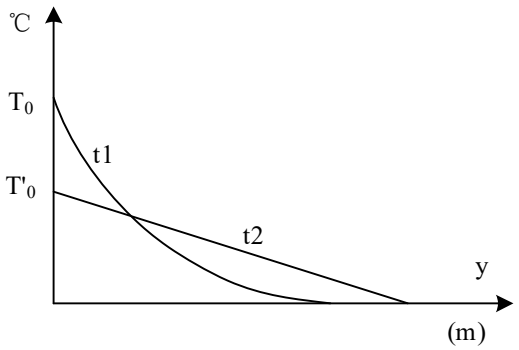

Figure 7: Nonlinear temperature difference calculation

Assume that $t_1 = T_0 e^{-ay}$ is the actual bending deformation of the box girder due to temperature difference with radius of curvature ρ_1 and $t_2 = T_0' \frac{h-y}{h}$ is the equivalent bending deformation due to temperature difference with radius of curvature ρ_2. From $\frac{\varepsilon_2}{h} = \frac{\alpha T_0}{I}[bk_4 - b_0c_4 + 2b\gamma_4]$, and $\frac{1}{rho_1} = \frac{\varepsilon_2}{h}$,

Get:

$$\frac{1}{\rho_1}\frac{\varepsilon_2}{h}=\frac{\alpha T_0}{I}\left[bk_4-b_0c_4+2b\gamma_4\right],\frac{1}{\rho_2}=-\frac{\alpha T_0'}{h} \tag{24}$$

Assuming that $T_0'=\mu T_0$.

Then:

$$\mu_0=-\frac{h}{I}\left[bk_4-b_0c_4+2b\gamma_4\right]=-\frac{h}{I}\eta_2 \tag{25}$$

(4) Transverse temperature difference stress

Transverse temperature difference stress includes transverse self-contained stress and transverse frame-contained stress, and both will cause longitudinal cracks in the beam. Its calculation formula is as follows:

The transverse frame restraint temperature difference stress can be calculated by the theoretical method of structural mechanics:

$$\begin{aligned}x_1\delta_{11}+x_1\delta_{11}+\Delta_1 t=0\\ x_2\delta_{21}+x_2\delta_{22}+\Delta_2 t=0\end{aligned} \tag{26}$$

Substituting the coefficients gives the calculation:

$$\begin{aligned}x_1&=\frac{\gamma(3\gamma+2)\alpha T_0 EK}{(\gamma+1)(3\gamma+1)}\frac{I}{\delta}\\ x_2&=-\frac{3\gamma\alpha T_0 EK}{(3\gamma+1)}\frac{I}{\delta}\end{aligned} \tag{27}$$

The lateral confining stress in the top plate is:

$$\sigma_2=\pm\frac{\gamma(3\gamma+2)\alpha T_0 EK}{(\gamma+1)(3\gamma+1)} \tag{28}$$

The lateral confining stress in the bottom plate is:

$$\sigma_2=\pm\frac{\gamma\alpha T_0 EK}{(\gamma+1)(3\gamma+1)} \tag{29}$$

As known from the principle of reinforced concrete design, the longitudinal ultimate tensile strength of concrete material is much higher than the transverse ultimate tensile strength, and the force of the structure is biased towards insecurity if the bridge specification strength value is directly followed in the calculation for comparison.

III. Construction control and parameter sensitivity analysis of mid-span merging of asymmetric structure of the bridge

Through the asymmetric load monitoring method and mechanical analysis model based on machine vision established in Chapter 2, this chapter takes Bridge A as the engineering background, combines the construction characteristics of its asymmetric structure with mid-span merging, further verifies the applicability of the theoretical model, and launches a systematic study on the force of the main pier, the effect of the top thrust force and the sensitivity of the construction parameters, so as to provide technical support for the actual project.

III. A. Analysis of force characteristics of main pier and control strategy of top thrust force

III. A. 1) Analysis of control main piers

Due to the main bridge for the asymmetric structure, the internal force for the asymmetric form, the two main piers of the bridge control cross-section force comparison, analyze the relatively unfavorable force of the main pier and its pier top horizontal displacement for the control amount of the top thrust force. Considering the shrinkage and creep after the bridge is completed, the comparison of the internal force and stress of the control section of the two main piers by permanent action is listed in Table 1.

Table 1: Comparison of internal forces and stresses on the main fault control surfaces

Section number	Pier number	Bending moment(kN·m)	Axial force(kN)	Shear force(kN)	Upper edge stress(MPa)	Lower edge stress(MPa)
A	50# (West side)	17075	-37086	-2957	0.92	-5.48
	51# (East Side)	-16993	-39301	3025	0.87	-5.57
B	50# (West side)	10886	-60200	-1941	-2.57	-3.98
	51# (East Side)	-10747	-57116	1875	-2.95	-3.95
C	50# (West side)	-14227	-42742	-3407	-4.69	1.02
	51# (East Side)	14595	-46008	3345	-4.19	0.88
D	50# (West side)	-5642	-81524	-805	-7.62	-2.69
	51# (East Side)	5464	-78694	854	-8.05	-2.71

Table 1 compares the internal force and stress distributions of the control sections of the main piers of Bridge A 50# (west side) and 51# (east side) after the bridge is completed. The data show that, except for section C, the bending moment of the west pier is generally larger than that of the east pier, e.g., the bending moment of the west pier of section A is 17075 kN·m, while that of the east pier is -16993 kN·m, which indicates that the west pier bears more loads in the positive moment section. From the stress distribution, section A and C of the upper and lower edges of the tensile stress, the west side of the pier section A of the upper edge of the tensile stress of 0.92 MPa, slightly higher than the east side of the pier of 0.87 MPa; and the west side of the pier of the compressive stress in the B, D section is more significant, the west side of the section D of the lower edge of the compressive stress is -2.69 MPa, the east side of the -2.71 MPa. Comprehensive analysis shows that the west pier more unfavorable, the top horizontal displacement of the pier should be used as the basis for the load, and the west pier is more unfavorable. It is necessary to use the horizontal displacement of the top of the pier as a control quantity, and the finalized top thrust force is 7812 kN.

Due to the asymmetry of bridge A is not very significant, the above data comparison difference is relatively small, if the asymmetry of the span of the difference is larger, it can be more obvious to derive the results of the above analysis. In addition, it can provide a certain reference basis for this type of bridge, three-span asymmetric continuous rigid bridge top thrust in the middle span near the side span diameter of the smaller side of the main pier pier top horizontal displacement as a control quantity.

III. A. 2) Comparison before and after jacking

After clarifying the force characteristics of the main pier and determining the control amount of the jacking force, it is necessary to further analyze the actual effects of the jacking force on the internal forces of the main girder and the main pier. For this reason, this section compares the internal force and stress distribution in the control section of the main girder before and after applying the jacking force to quantify the optimization effect of the jacking force on the structural forces.

The comparison of the internal forces and stresses in the control section of the main girder with and without the permanent action of the thrust is shown in Table 2, considering the shrinkage creep after the bridge is completed.

Table 2: Comparison of internal forces and stresses in sections with/without top thrust

Section number	Working condition	Bending moment(kN·m)	Axial force(kN)	Shear force(kN)	Upper edge stress(MPa)	Lower edge stress(MPa)
1	Without top thrust	-21243	-138068	5022	-7.15	-8.07
	With top thrust	429	-137135	4339	-7.45	-7.59
2	Without top thrust	-135302	-344517	38996	-5.49	-8.04
	With top thrust	-86499	-343467	37173	-5.98	-7.43
3	Without top thrust	-126388	-297322	-50714	-5.92	-10.16
	With top thrust	-103260	-283196	-50171	-6.11	-10.19
4	Without top thrust	363	-106462	217	-7.77	-7.02
	With top thrust	-965	-115411	217	-8.01	-7.66

Table 2 compares the effects of the presence or absence of the jacking force on the internal forces and stresses in the control section of the main beam. The effect of the jacking force on the axial force and shear force is small, e.g., the axial force of section 1 changes from -138068 kN to -137135 kN, and the shear force of section 1 decreases from 5022 kN to 4339 kN, but the adjusting effect on the bending moment is significant. For example, the section 1

bending moment reverses from -21243 kN·m without jacking to 429 kN·m with jacking, indicating that the jacking force effectively reduces the load in the negative moment section through eccentricity. In terms of stress, the jacking force increases the compressive stress at the upper edge of some sections, e.g., the stress at the upper edge of section 1 increases from -7.15 MPa to -7.45 MPa, and at the same time, the compressive stress at the lower edge decreases, e.g., the stress at the lower edge of section 1 decreases from -8.07 MPa to -7.59 MPa, which overall equalizes the stresses on the cross-section of the main girder. The mid-span section 4 is less affected by the top thrust, but the bending moments of the rest of the sections are optimized significantly, which verifies the effectiveness of the top thrust in improving the force distribution of the main girder.

The following is just to reflect the effect of the top thrust on the main pier only listed in the 50 # (west) pier comparison results; into the bridge after the consideration of shrinkage creep, with or without the top thrust conditions of permanent action on the 50 # (west) pier control cross-section of the internal force and stress comparison is listed in Table 3.

Table 3: Comparison of control section force of 50# pier with and without top thrust

Section number	Working condition	Bending moment(kN·m)	Axial force(kN)	Shear force(kN)	Upper edge stress(MPa)	Lower edge stress(MPa)
A	Without top thrust	-18082	-31857	-4497	0.83	-5.54
	With top thrust	2613	-34089	-834	-2.12	-3.22
B	Without top thrust	-3256	-57262	-780	-3.39	-5.06
	With top thrust	14260	-53015	1228	-5.84	-1.21
C	Without top thrust	20043	-40611	2043	-5.88	0.87
	With top thrust	-638	-78178	187	-3.77	-3.32
D	Without top thrust	13443	-80169	-2182	-8.47	-2.02
	With top thrust	-3765	-78151	797	-3.14	-4.26

Table 3 focuses on the influence of jacking thrust on the control section of the 50# (west) main pier. The bending moment distribution of section B is reversed from -3256 kN·m to 14260 kN·m, and the bending moment of section D is reduced from 13443 kN·m to -3765 kN·m, indicating that the top thrust weakens the eccentric force of the main pier through horizontal action. The change of shear force is more obvious, for example, the shear force of cross-section A decreases from -4497 kN to -834 kN, while the axial force of cross-section A increases from -31857 kN to -34089 kN. In terms of stress, the thrust eliminates the tensile stress of the A and C sections of the west pier, the stress at the upper edge of section A changes from 0.83 MPa to -2.12 MPa, and the compressive stress distribution is more balanced, and the stress at the lower edge of section B is improved from -5.06 MPa to -1.21 MPa. The data show that the jacking force not only reduces the horizontal displacement of the pier top, but also optimizes the stress state of the main pier, making it more in line with the safety design requirements.

In summary, the jacking force applied before the mid-span merging can adjust the structural internal force and improve the structural stress; the jacking force can not only reduce the horizontal displacement of the top of the pier, but also effectively improve the force of the main pier and the main girder, so that the structural stress tends to be more reasonable; however, the optimization effect of the jacking force on the force of the main pier is greater than that of the force of the main girder. In addition, the horizontal jacking force can reduce the deflection angle of the main pier to the center of the span and thus curb the downward deflection of the main girder.

III. B. Analysis of the effect of the molecular resistance coefficient μ of the reserved pipe on the deflection

After verifying the effectiveness of the jacking force on the adjustment of the structural force, the study further explores the influence of construction parameters on the deflection of the bridge. By analyzing the sensitivity of the resistance coefficient of the reserved pipe, the study reveals its differentiated effect on the displacement of the main girder in the maximum cantilever state and the bridge-forming state, which provides a theoretical basis for the control of the construction accuracy.

The difference in displacement of each node of the main girder at the maximum cantilever state and bridge-forming state with ±5% and 10% change in the coefficient of friction is shown in Fig. 8 and Fig. 9, respectively.

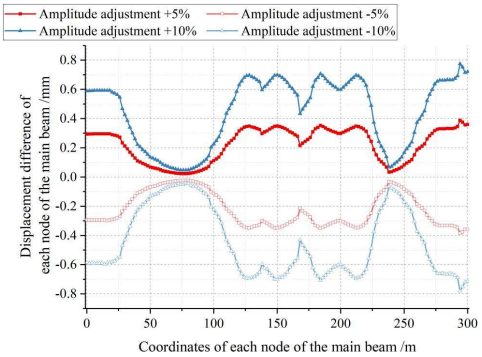

Figure 8: Displacement difference of friction coefficient changes at cantilever state

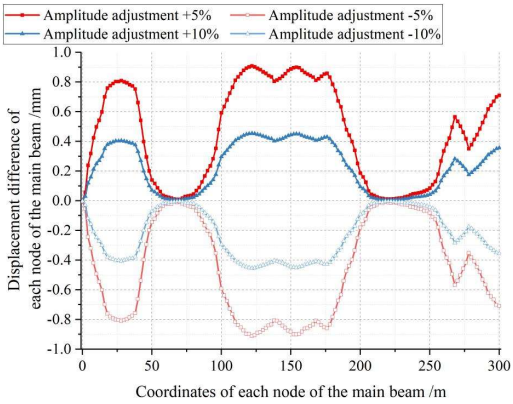

Figure 9: Displacement difference of friction coefficient changes at completed state

From Figures 8 and 9, it can be seen that whether it is the maximum cantilever state or the bridge-forming state, the prestressing pipe mooring coefficient fluctuates up and down by 5% and 10%, which leads to the change of the magnitude of the prestressing force of the steel bundles, and the displacement difference of each node of the main girder is symmetrically distributed with respect to the design state. In the maximum cantilever state, the absolute changes of the displacement difference are 0.36mm and 0.72mm for 5% and 10% fluctuation of the modulus, and the absolute changes of the displacement difference are 0.46 and 0.92mm for the bridge state, and the maximum displacement difference of both of them occurs near the maximum cantilever at the middle of the main span. It seems that the variation of 5% and 10% of the prestressing pipe mooring coefficient has a certain effect on the deflection of the main girder, but the effect on the bridge-forming condition is greater compared with that of the maximum cantilever condition.

IV. Conclusion

In this study, the stress and deflection response of bridge construction under asymmetric loading is systematically analyzed by integrating machine vision technology and mechanics theory, and the validity of the method is verified by using A bridge as an engineering case.

The cable-force ratio model derived from the mechanical equilibrium equation shows that the cable-force ratio between the railway side and the highway side is 1.71. After the jacking force of 7812 kN is applied, the force of the main pier is significantly optimized, the bending moment of section B of the 50# pier is reversed from -3256 kN·m to 14260 kN·m, and the tensile stress of the upper edge of section A is reduced from 0.83 MPa to -2.12 MPa, which completely eliminates the risk of eccentric stress. The bending moment of the main beam cross-section 1 is reversed from -21243 kN·m to 429 kN·m, and the adjustment range is 98%, which verifies the key role of jacking force in improving the structural stress. When the friction coefficient of the reserved pipeline fluctuates by ± 10%, the maximum displacement difference in the middle span of the main girder in the bridged state is 0.92 mm, and the cantilever state is 0.72 mm, which highlights the sensitivity of the construction parameters to the deflection control.

References

[1] Zhao, R., Yuan, Y., Wei, X., Shen, R., Zheng, K., Qian, Y., ... & Yu, C. (2020). Review of annual progress of bridge engineering in 2019. Advances in Bridge Engineering, 1, 1-57.

[2] Qin, S., & Gao, Z. (2017). Developments and prospects of long-span high-speed railway bridge technologies in China. Engineering, 3(6), 787-794.
[3] Yan, B., Dai, G. L., & Hu, N. (2015). Recent development of design and construction of short span high-speed railway bridges in China. Engineering Structures, 100, 707-717.
[4] Zhou, G. D., Yi, T. H., Li, W. J., Zhong, J. W., & Zhang, G. H. (2020). Standardization construction and development trend of bridge health monitoring systems in China. Advances in Bridge Engineering, 1, 1-18.
[5] Zheng, J. (2024). Recent construction technology innovations and practices for large-span arch bridges in China. Engineering, 41, 110-129.
[6] Lipták, I., Kopáčik, A., Erdélyi, J., & Kyrinovič, P. (2013). Dynamic deformation monitoring of bridge structure. Selected Scientific Papers-Journal of Civil Engineering, 8(2), 13-20.
[7] Erdélyi, J., Kopáčik, A., & Kyrinovič, P. (2020). Spatial data analysis for deformation monitoring of bridge structures. Applied Sciences, 10(23), 8731.
[8] Rizzo, P., & Enshaeian, A. (2021). Challenges in bridge health monitoring: A review. Sensors, 21(13), 4336.
[9] Jiang, S., Zhang, J., & Gao, C. (2023). Bridge Deformation Measurement Using Unmanned Aerial Dual Camera and Learning‐Based Tracking Method. Structural Control and Health Monitoring, 2023(1), 4752072.
[10] Qin, X., Zhang, L., Yang, M., Luo, H., Liao, M., & Ding, X. (2018). Mapping surface deformation and thermal dilation of arch bridges by structure-driven multi-temporal DInSAR analysis. Remote sensing of environment, 216, 71-90.
[11] Zhang, Q. H., Bu, Y. Z., & Li, Q. (2017). Review on fatigue problems of orthotropic steel bridge deck. China Journal of Highway and Transport, 30(3), 14-30.
[12] Li, C., Yao, Y., Li, Z., & Ji, B. (2025). Study on the Impact of Diaphragm Deformation on Fatigue Performance and Maintenance Strategies in Steel Bridge Decks. Applied Sciences, 15(8), 4245.
[13] Di, J., Ruan, X., Zhou, X., Wang, J., & Peng, X. (2021). Fatigue assessment of orthotropic steel bridge decks based on strain monitoring data. Engineering structures, 228, 111437.
[14] Ye, X. W., Su, Y. H., & Xi, P. S. (2018). Statistical analysis of stress signals from bridge monitoring by FBG system. Sensors, 18(2), 491.
[15] Meng, X., Nguyen, D. T., Xie, Y., Owen, J. S., Psimoulis, P., Ince, S., ... & Bhatia, P. (2018). Design and implementation of a new system for large bridge monitoring—GeoSHM. Sensors, 18(3), 775.
[16] He, Z., Li, W., Salehi, H., Zhang, H., Zhou, H., & Jiao, P. (2022). Integrated structural health monitoring in bridge engineering. Automation in construction, 136, 104168.
[17] Ghahremani, B., Enshaeian, A., & Rizzo, P. (2022). Bridge health monitoring using strain data and high-fidelity finite element analysis. Sensors, 22(14), 5172.
[18] Chen, Z. W., Zhu, S., Xu, Y. L., Li, Q., & Cai, Q. L. (2015). Damage detection in long suspension bridges using stress influence lines. Journal of Bridge Engineering, 20(3), 05014013.
[19] Catbas, N., Dong, C. Z., Celik, O., & Khuc, T. (2018, July). A vision for vision-based technologies for bridge health monitoring. In Maintenance, Safety, Risk, Management and Life-Cycle Performance of Bridges. Proceedings of the Ninth International Conference on Bridge Maintenance, Safety and Management (IABMAS 2018) (pp. 54-62). Melbourne, Australia: CRC Press/Balkema.
[20] Ye, X. W., Dong, C. Z., & Liu, T. (2016). A review of machine vision‐based structural health monitoring: methodologies and applications. Journal of Sensors, 2016(1), 7103039.
[21] Ge, L., Dan, D., Liu, Z., & Ruan, X. (2022). Intelligent simulation method of bridge traffic flow load combining machine vision and weigh-in-motion monitoring. IEEE Transactions on Intelligent Transportation Systems, 23(9), 15313-15328.
[22] Dan, D., Ying, Y., & Ge, L. (2021). Digital twin system of bridges group based on machine vision fusion monitoring of bridge traffic load. IEEE Transactions on Intelligent Transportation Systems, 23(11), 22190-22205.
[23] Obiechefu, C. B., & Kromanis, R. (2021). Damage detection techniques for structural health monitoring of bridges from computer vision derived parameters. Structural Monitoring and Maintenance, 8(1), 91-110.
[24] Gomez-Cabrera, A., & Escamilla-Ambrosio, P. J. (2022). Review of machine-learning techniques applied to structural health monitoring systems for building and bridge structures. Applied Sciences, 12(21), 10754.
[25] Lydon, D., Taylor, S., Lydon, M., del Rincon, J. M., & Hester, D. (2019). Development and testing of a composite system for bridge health monitoring utilising computer vision and deep learning. Smart Structures and Systems, 24(6), 723-732.